

Comparison of performance limits of the HOT HgCdTe photodiodes with colloidal quantum dot infrared detectors

A. ROGALSKI¹, M. KOPYTKO^{1*}, P. MARTYNIUK¹, and W. HU²

¹Institute of Applied Physics, Military University of Technology, ul. Kaliskiego 2, 00-908 Warsaw, Poland

²State Key Laboratory of Infrared Physics, Shanghai Institute of Technical Physics, Chinese Academy of Sciences, 500 Yu Tian Road, Shanghai 200083, China

Abstract. In the past decade, there has been significant progress in development of the colloidal quantum dot (CQD) photodetectors. The CQD's potential advantages include: cheap and easy fabrications, size-tuneable across wide infrared spectral region, and direct coating on silicon electronics for imaging, which potentially reduces array cost and offers new modifications like flexible infrared detectors. The performance of CQD high operating temperature (HOT) photodetectors is lower in comparison with detectors traditionally available on the global market (InGaAs, HgCdTe and type-II superlattices). In several papers their performance is compared with the semiempirical rule, "Rule 07" (specified in 2007) for P-on-n HgCdTe photodiodes. However, at present stage of technology, the fully-depleted background limited HgCdTe photodiodes can achieve the level of room-temperature dark current considerably lower than predicted by Rule 07. In this paper, the performance of HOT CQD photodetectors is compared with that predicted for depleted P-i-N HgCdTe photodiodes. Theoretical estimations are collated with experimental data for both HgCdTe photodiodes and CQD detectors. The presented estimates provide further encouragement for achieving low-cost and high performance MWIR and LWIR HgCdTe focal plane arrays operating in HOT conditions.

Key words: colloidal quantum dot infrared photodetectors, HOT infrared detectors, HgCdTe photodiodes, P-i-N depleted photodiodes, BLIP performance.

1. Introduction

It is true that infrared (IR) detectors trace their origins to 11th February 1800 when John Frederik William Herschel's experimented with thermometer on refraction of invisible rays using a prism. The first IR detection systems in XIX century were based on thermal detectors: thermometers, thermocouples, and bolometers. The development of IR photon detector technology began around 1930 and was dominated from the beginning by photoemissive photocathodes and lead salt photoconductors. Lead sulphide photoconductors were brought to the manufacturing stage in Germany in about 1943. However, the development of modern IR detectors became possible after the invention of a transistor in December 23, 1947 at Bell Laboratories in Murray Hill, New Jersey, by William Shockley, John Bardeen and Walter Brattain (see Fig. 1). In the next decade Ge, Si, InSb and HgCdTe photon detectors were developed. In 1956 Texas Instruments began research on IR technology which led to the signing of several contracts with a linear scanner and the invention of the first forward-looking infrared (FLIR) camera in 1963. In 1972, Texas Instruments invented the Common Module concept, which contributed to a significant cost reduction and allowed for the reuse of common components. These systems belong to the so called first generation scanning systems.

HgCdTe inspired the development of the three "generations" of detectors considered for the military and civilian applications and shortly described in the caption of Fig. 1. The IR detector technology combined with fabrication of epitaxial heterostructure [by molecular beam epitaxy (MBE) and metalorganic chemical vapour deposition (MOCVD)] and photolithographic processes revolutionized the semiconductor industry, thus enabling the design and fabrication of the complex focal plane arrays (FPAs). The further development will be connected with the implementation of fourth generation staring systems, whose the main features are to be: high resolution (with a very large number of pixels – above 10^8), multi-colour functionality, three dimensional readout integration circuits (3D ROIC), and other integration functions; e.g. better radiation/pixel coupling, avalanche multiplication in pixels, and polarization/phase sensitivity. The first three generations of the imaging systems rely primarily on the planar FPAs. Several methods to overcome these limitations, including the detectors bonding to flexible or curved molds, have been proposed [1]. Evolution of fourth generation is inspired by the most famous visual systems, which are the biological eyes. The solution based on the Petzval-matched curvature allows the reduction of field curvature aberration. In addition, it combines such advantages as simplified lens system, electronic eye systems and wide field-of-view [2, 3]. The colloidal quantum dot (CQD) and 2D layered material are promising materials to overcome technical challenges in the development of fourth generation IR systems [4].

Theoretical estimates carried out by Martyniuk et al. [5] in 2008 indicate that the self-assembled quantum dot infrared

*e-mail: malgorzata.kopytko@wat.edu.pl

Manuscript submitted 2020-02-14, initially accepted for publication 2020-03-28, published in August 2020

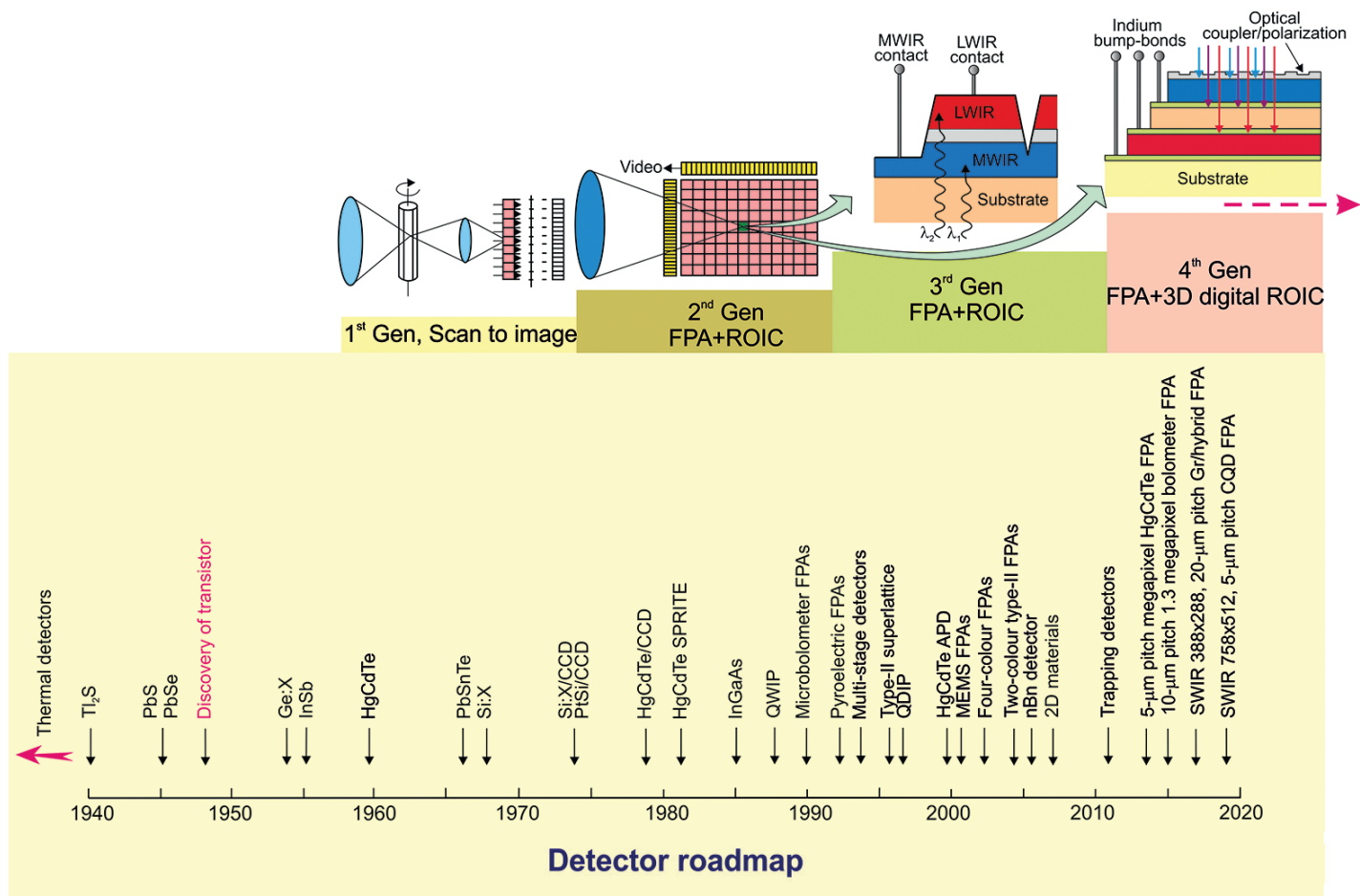


Fig. 1. The development of IR detectors and systems history. For principal military and civilian applications four generation systems can be considered: first generation (scanning systems), second generation (staring systems – electronically scanned), third generation (staring systems with large number of pixels and two-colour functionality), and fourth generation (staring systems with very large number of pixels, multi-colour functionality, 3D ROIC, and other on-chip functions; e.g. better radiation/pixel coupling, avalanche multiplication in pixels, polarization/phase sensitivity)

photodetectors (QDIPs) are suitable for noncryogenic operation especially in long-wavelength infrared (LWIR) region. In practice however, the reduced performance of QDIP is the result of nonoptimal band structure and technological problems such as QD size and density control. More recently, the attractive alternative to self-assembled epitaxial QDs has been CQDs with better size tunability of optical features and reduction of fabrication cost.

At present stage of technology, the performance of CQD high operating temperature (HOT) photodetectors is still lower in comparison with traditional detectors existing on the global market (InGaAs, HgCdTe and type-II superlattices – T2SLs). In several papers their performance is compared with the semiempirical rule, “Rule 07” (specified in 2007) for P-on-n HgCdTe photodiodes. However, the depleted background limited HgCdTe photodiodes can achieve the level of room-temperature dark current considerably lower than predicted by Rule 07 [6]. From these reasons, in the present paper, the performance of HOT CQD HOT photodetectors is compared with that predicted for depleted P-i-N HgCdTe photodiodes.

Theoretical estimates are collated with experimental data for both HgCdTe photodiodes and CQD detectors.

2. Brief view on CQD photodetectors

In the last decade, a significant progress in fabrication of CQD photodetectors has been observed. In this approach, an active region is constructed based on 3D quantum confined semiconductor nanoparticles synthesized by inorganic chemistry. CQDs offer a promising alternative to the single crystal IR materials (InGaAs, InSb, InAsSb, HgCdTe, as well as T2SLs). These nanoparticles could improve CQD photodetectors performance compared to epitaxial QDs due to many aspects gathered in Table 1 [7, 8].

CQDs offer an alternative for near/short-wave/mid-wave infrared (NIR/SWIR/MWIR) imaging (see Fig. 2). Typically CQD photodetectors are fabricated using conducting-polymer/nanocrystal blends, or nanocomposites [8–12]. Nanocomposites often feature narrow-bandgap, II–VI (HgTe, HgSe) [13–15],

Table 1
 Advantages and disadvantages of CQD photodetectors in comparison with single crystal QD photodetectors

Advantages	Disadvantages
<ul style="list-style-type: none"> • control of dot synthesis and absorption spectrum by ability of QD size-filtering, which leads to highly-uniform ensembles • much stronger absorption than in Stranski-Krastanov grown QD due to close-packed CDs • considerable elimination of strains influencing the growth of epitaxial QDs by greater selection of active region materials • reduction of cost fabrication (using e.g. such solution as spin coating, inject printing, doctor blade or roll-to-roll printing) compared to epitaxial growth • deposition methods are compatible with a variety of flexible substrates and sensing technologies such as CMOS (e.g. direct coating on silicone electronics for imaging) 	<ul style="list-style-type: none"> • inferior chemical stability and electronic passivation of the nanomaterials in comparison with epitaxial materials • bipolar, interband (or excitonic) transitions across the CQD bandgap (e.g. electrons hopping among QDs and holes transport through the polymer) contrary to the intraband transitions in the epitaxial QDs • insulating behaviour due to slow electron transfer through many barrier interfaces in a nanomaterial • problems with long term stability due to the large density of interfaces with atoms presenting different or weaker binding • high level of 1/f noise due to disordered granular systems

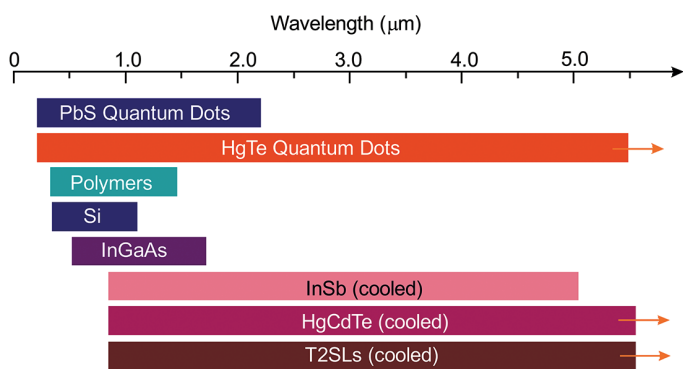


Fig. 2. The wavelengths range that can be detected by materials commonly used in imaging applications

PbSe or PbS [16–19] colloidal QDs. Usually, the reported IR photodetectors use colloidal QDs embedded in conducting polymer matrices, such as poly [2-methoxy-5-(2-ethylhexyloxy)-1,4-phenylenevinylene] (MEH-PPV).

It is expected that the extension of application of CQD-based devices will be significant, especially in the area of IR imaging which is currently dominated by epitaxial semiconductor and hybrid technologies [20]. Hybrid technology, due to the complexity of production stages, reduces yield and increases overall cost. The IR CQD-based photodetectors are an alternative solution without these limitations.

The CQD layers are amorphous which permits fabrication of devices directly onto ROIC substrates, as shown in Fig. 3, with no restrictions on pixel or array size and with a day cycle of production. In addition, the monolithic integration of CQD detectors into ROIC does not require any hybridization step. Individual pixels are defined by the area of the metal pads arranged on the top of ROIC surface. To synthesize colloidal nanocrystals, wet chemistry techniques are used. Reagents are injected into a flask and, the desirable shape and size of nanocrystals are obtained by the control of reagent concentrations, ligand selection, and temperature. This so called top-surface photodetector offers a 100% fill factor and is compatible with postprocessing at the top of CMOS electronics.

From a performance standpoint, SWIR photodetectors based on PbS CQDs have achieved detectivities (D^*) comparable to commercial InGaAs photodiodes, with values of $>10^{12}$ Jones at 300 K. D^* between 10^{10} to 10^9 Jones at 5- μm was demonstrated for HgTe CQD devices while maintaining a fast response time at thermoelectric cooling temperatures. It is unlikely that CQD IR detectors will ever achieve the performance of currently popular InGaAs, HgCdTe, InSb and T2SL photodiodes. However, recent demonstration of low-cost SWIR and MWIR CQD imaging arrays have heightened the interest in these devices. It is expected that the successful implementation of this new class of IR technology may match the broad impact of cheap CMOS cameras that are widely used today. First SWIR infrared cameras built on CQD thin film photodiodes fabricated monolithically

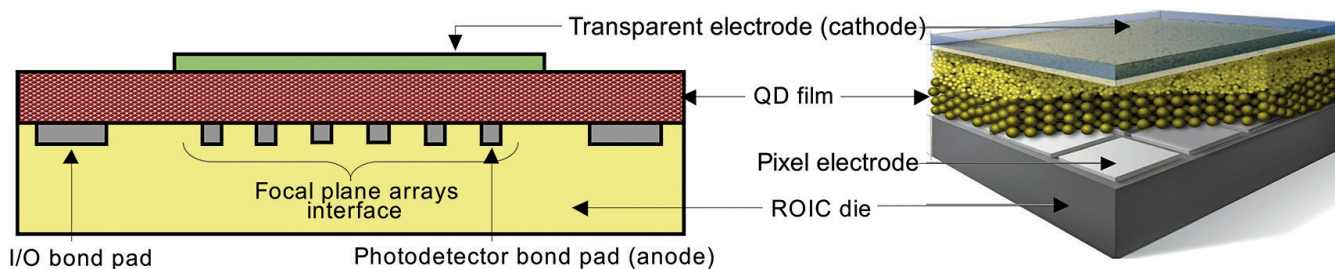


Fig. 3. Infrared monolithic array structure based on CQDs (after Ref. 8)

cally on silicon readout integrated circuits have been launched [21, 22]. The Acuros camera has the resolution of 1920×1080 (2.1 megapixels, 15- μm pixel pitch) and uses 0.4 to 1.7 μm roadband spectral response [21]. The IMEC's prototype imager has the resolution of 758×512 pixels and 5- μm pixel pitch. The CQD photodiodes on the silicon substrate achieve an external quantum efficiency of above 60% at 940 nm wavelength, and above 20% at 1450 nm, allowing uncooled operation with dark current comparable to commercial InGaAs photodetectors [22]. At present, CQD cameras are used in newer applications that require high definition low cost imaging on smaller pixels without extreme sensitivity. It can be predicted that increasing the dot size while maintaining a good mono-dispersion, carrier transport and quantum efficiency (QE) will improve maintaining low noise levels. Due to continuous development of deposition and synthesis techniques, much higher performances will be achieved in the future.

3. Trends in IR HOT photodetectors

In 1999 the famous British scientist Tom Elliott and his co-workers wrote that *there is no fundamental obstacle to obtaining room temperature operation of photon detectors at room temperature with background-limited performance even in reduced fields of view* [23]. The invention of microbolometer array was a milestone step in the development of IR cameras operating at room temperature. However, microbolometer belongs to class of thermal detectors with limited response time – typically in millisecond range. To omit this limitation, further efforts are directed to increase operating temperature of photon detectors.

The present efforts in IR detector technologies are particularly addressed to decrease imaging system size, weight, and power consumption (SWaP), which consequently leads to a system's cost reduction and to increase the operating temperature [24, 25]. The ultimate goal is the fabrication of HOT photodetector characterized by the dark current less than the system background flux current and with $1/f$ noise negligibly small in comparison to the shot noise of the background flux.

In several papers it was shown that the detector size, d , and F -number ($f/\#$) are basic parameters of IR systems [26, 27]. Since they depend on $F\lambda/d$ (where λ is the wavelength), these two parameters have great impact on the detection/identification range, as well as the noise equivalent difference temperature ($NEDT$), [27]:

$$\text{Range} = \frac{D\Delta x}{M\lambda} \left(\frac{F\lambda}{d} \right), \quad (1)$$

$$NEDT = \frac{2}{C\lambda (\eta\Phi_B^{2\pi} \tau_{int})} \left(\frac{F\lambda}{d} \right). \quad (2)$$

Here D is the aperture, M is the number of pixels required to identify a target Δx , C is the scene contrast, η is the detector collection efficiency, $\Phi_B^{2\pi}$ is the background flux into a 2π FOV, and τ_{int} is the integration time. The relations (1) and (2) allow to conclude that the space defined parameter by $F\lambda$ and d may

be used in the optimal design of any IR system. As is shown in [28], for IR systems with $f/1$ optics, the smallest usable detector size should be 2 μm and 5 μm for the MWIR and LWIR range, respectively. With more realistic $f/1.2$ optics, the smallest usable detector size is 3 μm in the MWIR and 6 μm in the LWIR.

It is well known and can be repeated after Kinch [27] that: *the ultimate cost reduction for an IR system will only be achieved by the room temperature operation of depletion-current limited arrays with pixel densities that are fully consistent with background and diffraction-limited performance due to the system optics*. The depletion-current limited P-i-N photodiodes demand long Shockley-Read-Hall (SRH) carrier lifetime, marked as τ_{SRH} , to meet the requirements of a low dark current. The long SRH lifetime of HgCdTe makes this material a great candidate for room-temperature operation [27].

The SRH generation-recombination mechanism determines the carrier lifetime in lightly doped n- and p-type HgCdTe, in which SRH centres are associated with residual impurities and native defects. The data gathered by Kinch et al. in 2005 [29] indicates that the measured values of carrier lifetimes for LWIR n-type HgCdTe range from 2 up to 20 μs at 77 K regardless of doping concentration for value below 10^{15} cm^{-3} . The values for MWIR material are typically slightly longer, in the range of 2–60 μs . However, several papers published in the last decade have shown τ_{SRH} considerably higher range in low temperature and low doping concentrations, above 200 μs up to even 50 ms depending on the cut-off wavelength [27] – see Table 2. The range of low doping that can be reproducibly generated in Teledyne growth HgCdTe epilayers by MBE is about 10^{13} cm^{-3} . In recently published paper by Gravrand et al. [30] it has been shown that for most tested MWIR photodiodes from Leti and Sofradir, the estimated SRH carrier lifetimes [from direct measurements (photoconductive or photoluminescence decay), as well as indirect estimates from current-voltage (I - V) characteristics], are in the range between 10 and 100 μs . These values are lower than previously estimated by US research groups. However, they were estimated for photodiodes with higher doping in the active region – above 10^{14} cm^{-3} . However, from just published results [31], Teledyne has confirmed fabrication of depletion layer limited P-i-N HgCdTe photodiodes with SRH recombination centres exhibiting lifetimes in the range 0.5–10 ms.

Table 2
Summary of the SRH carrier lifetimes determined on the basis of I - V and FPA characteristics (after Ref. 27)

	x composition	τ_{SRH} (μs)
LWIR	0.225	> 100 at 60 K
MWIR	0.30	> 1000 at 110 K
	0.30	~ 50000 at 89 K
SWIR	0.455	> 3000 at 180 K

All SRH lifetimes estimated for HgCdTe are usually carried out for temperature below 300 K. Their extrapolation to 300 K in order to predict the photodiode operation behaviour is questionable. In our estimates we assume τ_{SRH} equal 1 ms,

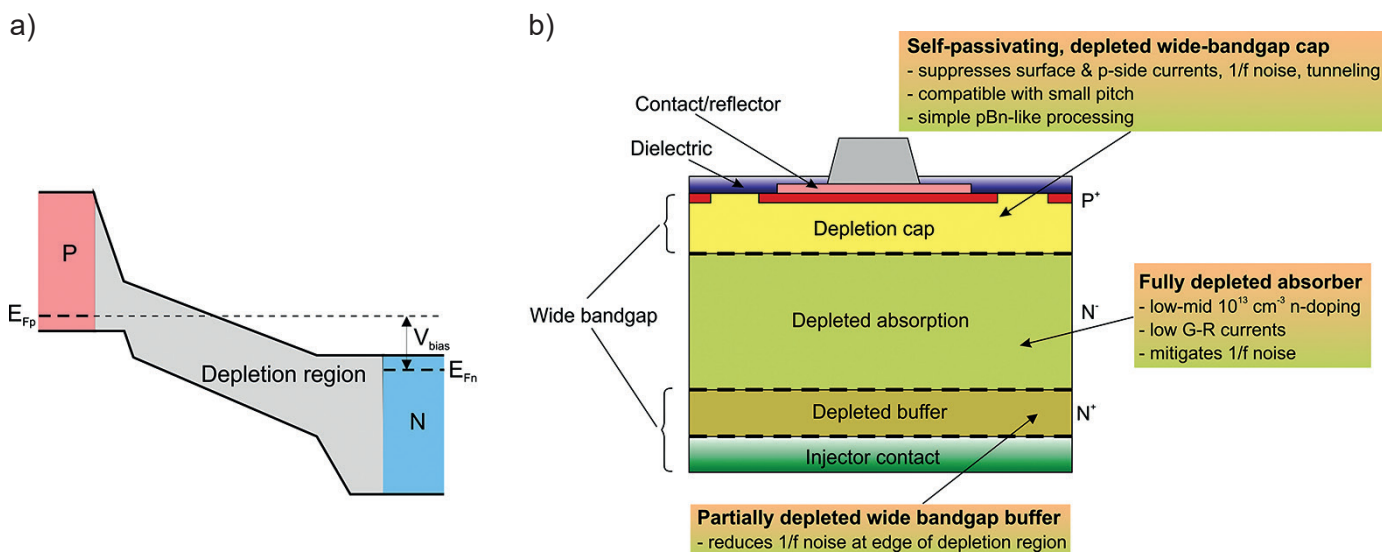


Fig. 4. P-i-N photodiode: a) energy band diagram under reverse bias, b) heterojunction architecture (adapted after Ref. 6)

which is supported by experimental data achieved by DRS and Teledyne research groups.

Figure 4a shows a schematic band diagram for a reverse biased P-i-N photodiode. The active region consists of an undoped i-region (v region, low n-doping) sandwiched between wider bandgap cap (P) and buffer (N) layers – see Fig. 4b [6]. Very low doping in the absorber (below $5 \times 10^{13} \text{ cm}^{-3}$) is required to allow full depletion at zero or low value of reverse bias. The surrounded wide-gap contact layers are designed to suppress the dark current generation from these regions and to suppress tunnelling current under reverse bias. Moreover, fully depleted absorber surrounded by wide bandgap regions potentially reduce 1/f and random telegraph noise. As previously mentioned, the fully-depleted P-i-N structure is compatible with the small pixel size, meeting the low crosstalk thanks to the built-in vertical electric field [6, 27].

In P-i-N design, the choice of absorber thickness should be a trade-off between the response speed and QE (or responsivity). To achieve short response times, the absorber thickness should be small and fully depleted. For high QE the absorption region should be thick enough to effectively collect photogenerated carriers. However, to enhance QE while maintaining high response speed, an external resonant microcavity has been proposed. In this approach, the absorber is placed inside a cavity so that a large portion of the photons can be absorbed even with small detection volume.

In general, for fully depleted P-i-N photodiode, the dark current is diffusion limited in N and P regions (dependent on SRH and Auger generations) and depletion limited by SRH generation in the space charge region. Influence of radiative recombination is still debatable but is not considered a limiting factor of small pixel HgCdTe photodiodes. Moreover, due to the photon recycling effect, the influence of radiative recombination can be significantly reduced [32]. Thus in our discussion the radiative recombination is omitted. If P-i-N photodiode operates under reverse bias, Auger suppression effect should

be taken into account. This effect is important above all in HOT condition when $n_i \gg N_{dop}$. In non-equilibrium a large number of intrinsic carriers can be swept-out from the absorber region. It is expected that this impact is larger for lower n-doping levels since n_i is proportionally higher. At very low level of n-type doping (about 10^{13} cm^{-3}) the ultimate performance of P-i-N photodiode is limited by SRH recombination and neither Auger recombination nor Auger suppression.

4. Analysis of photodetector structures and discussion

Below, we compare the doping dependence relation between diffusion and depletion currents for an ideal P-i-N HgCdTe photodiode including influence of Auger suppression under operation at non-equilibrium conditions. The considerations of P-i-N structure for operation at high temperatures are included in the Appendix.

The comparison of diffusion and depletion dark current components versus temperature for MWIR ($\lambda_c = 5 \mu\text{m}$) P-i-N photodiode, with the value of SRH carrier lifetime of 1 ms, absorber thickness of $5 \mu\text{m}$ and doping of $5 \times 10^{13} \text{ cm}^{-3}$ is presented in Fig. 5. The P-i-N HOT photodiode is characterized by useful properties at reverse bias operation. For the absorber doping level of $5 \times 10^{13} \text{ cm}^{-3}$, a $5\text{-}\mu\text{m}$ -thick absorber can be fully depleted at the reverse bias of 0.4 V (see Fig. A2). The diffusion component associated with Auger 1 mechanism is eliminated because of the absence of the majority carriers due to exclusion and extraction effects [33, 34]. The background radiation calculated from $f/3$ optics has decisive influence on dark current. It should be mentioned here, that the background flux current is defined by the total flux through the optics (limited by $f/\#$) plus the flux from the cold shield. This effect is shown by increasing influence of the background limited performance (BLIP) ($f/3$) on dark current at temperature above 220 K.

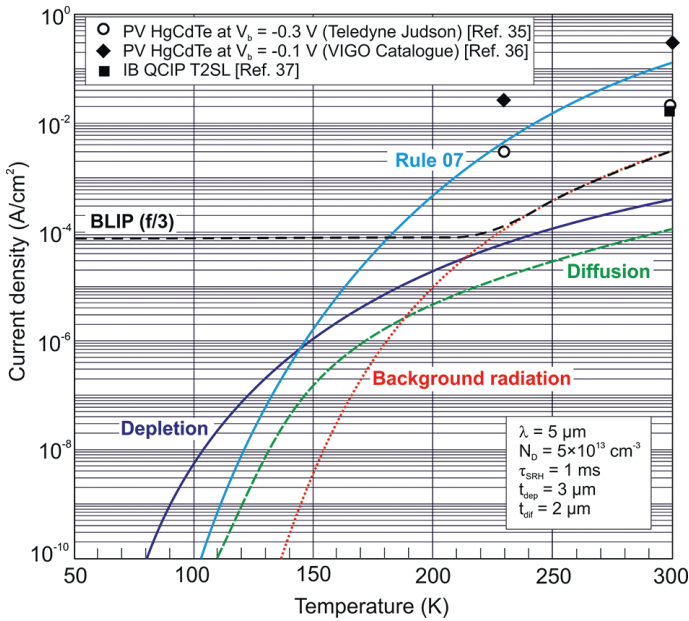


Fig. 5. Diffusion and depletion current components versus temperature for MWIR P-i-N photodiode with the value of $\tau_{SRH} = 1$ ms and absorber doping level of $5 \times 10^{13} \text{ cm}^{-3}$. The thickness of active region is $t = 5 \mu\text{m}$ and consists of $t_{dif} = 2 \mu\text{m}$ and $t_{dep} = 3 \mu\text{m}$. The experimental data are taken with different sources as marked. PC – photoconductor, PV – photodiode, IB QCIP – interband quantum cascade infrared photodetector

As is shown in Fig. 5, the Teledyne Judson experimentally measured current densities [35], at the bias of -0.3 V, are close to BLIP ($f/3$) curve – they are located less than one order of magnitude above this limit. The current density at room temperature is even lower than predicted by Rule 07. The measured current densities presented by VIGO are about one order of magnitude higher [36], however in this case they were measured at lower reverse bias, -0.1 V with less effective Auger contribution. It is interesting to notice, that the performance of interband quantum cascade infrared photodetectors (IB QCIP) based on T2SLs fabricated with InAs/GaSb coincide very well with upper experimental data for HgCdTe photodiodes at room temperature [37].

The photodiode specific detectivity, or D^* , is given on the basis of the current sensitivity R_i and the noise current density j_n in a 1-Hz bandwidth, and can be written as

$$D^* = \frac{R_i}{j_n} (\Delta f)^{\frac{1}{2}}. \quad (3)$$

For the non-equilibrium devices, the j_n value can be calculated including thermal Johnson Nyquist and optical and electrical shot noises using the following expression

$$j_n = \sqrt{(4k_B T / R_d A + 2qJ_{DARK} + 2qJ_{BLIP})}, \quad (4)$$

where k_B is the Boltzmann constant, $R_d A$ is the dynamic resistance area product, J_{DARK} and J_{BLIP} are the dark current density and the background induced current density, respectively.

D^* is expressed in units of $\text{cmHz}^{1/2}\text{W}^{-1}$, which recently has been referred to as “Jones”.

Figure 6 shows calculated detectivity versus temperature for MWIR P-i-N HgCdTe photodiode assuming identical parameters as taken in calculation presented in Fig. 5 ($\lambda_c = 5 \mu\text{m}$, $\tau_{SRH} = 1$ ms, $t = 5 \mu\text{m}$, $N_{dop} = 5 \times 10^{13}$). The current responsivity was calculated assuming of the $\text{QE} = 1$ (however typical QE reaches reasonable value of about 0.7). As shown, for MWIR photodiode with 5- μm cut-off wavelength and low doping in active region, D^* is limited by background and is about one order of magnitude higher than predicted by Rule 07. The experimental data given for HgCdTe photodiodes in Teledyne Judson and VIGO catalogues are more than one order of magnitude below background flux limitation for the $f/3$ optics. This comparison is less profitable for HgTe QD detectors with experimentally measured lower detectivities than for HgCdTe photodiodes.

Research on QD IR photodetectors based on self-assembled epitaxial QDs started in the mid 1990s and were initially very promising. As it happens later, that epitaxial QDs suffer from limited size control and low density of dots. Instead, the attractive alternative are CQDs due to their captivating size tunability of optical features and reduction of fabrication cost. The lead chalcogenides CQDs, primarily PbS, are the material to SWIR photodetectors with detection up to $2 \mu\text{m}$. The peak can be adjusted using smaller dots by adding NIR bands to hyperspectral visible image sensors or using larger dots to include the InGaAs spectrum of image sensors [19]. HgTe CQDs have opened the MWIR spectral range – see Figs. 7 and 8. For both

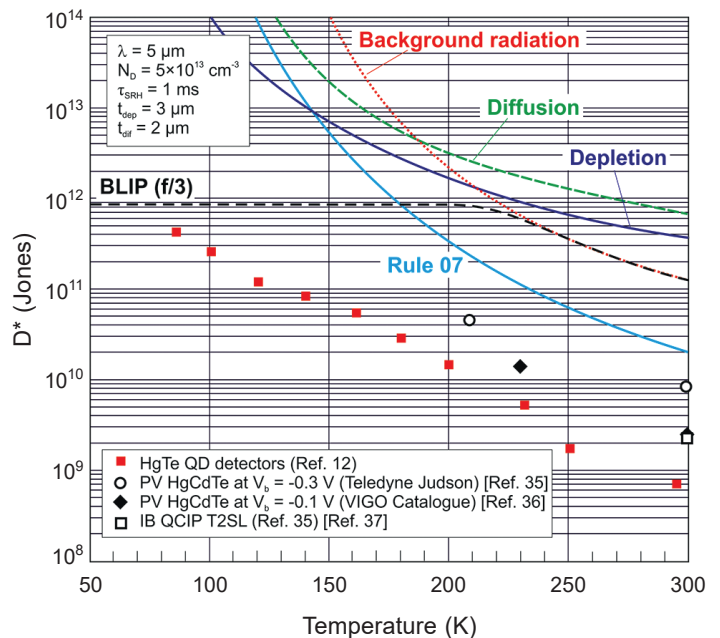


Fig. 6. Detectivity versus temperature for MWIR P-i-N photodiode with the value of $\tau_{SRH} = 1$ ms and absorber doping level of $5 \times 10^{13} \text{ cm}^{-3}$. Thickness of active region is $t = 5 \mu\text{m}$ and consists of $t_{dif} = 2 \mu\text{m}$ and $t_{dep} = 3 \mu\text{m}$. The experimental data are taken with different sources as marked. PC – photoconductor, PV – photodiode, IB QCIP – interband quantum cascade infrared photodetector

Comparison of performance limits of the HOT HgCdTe photodiodes with colloidal quantum dot infrared detectors

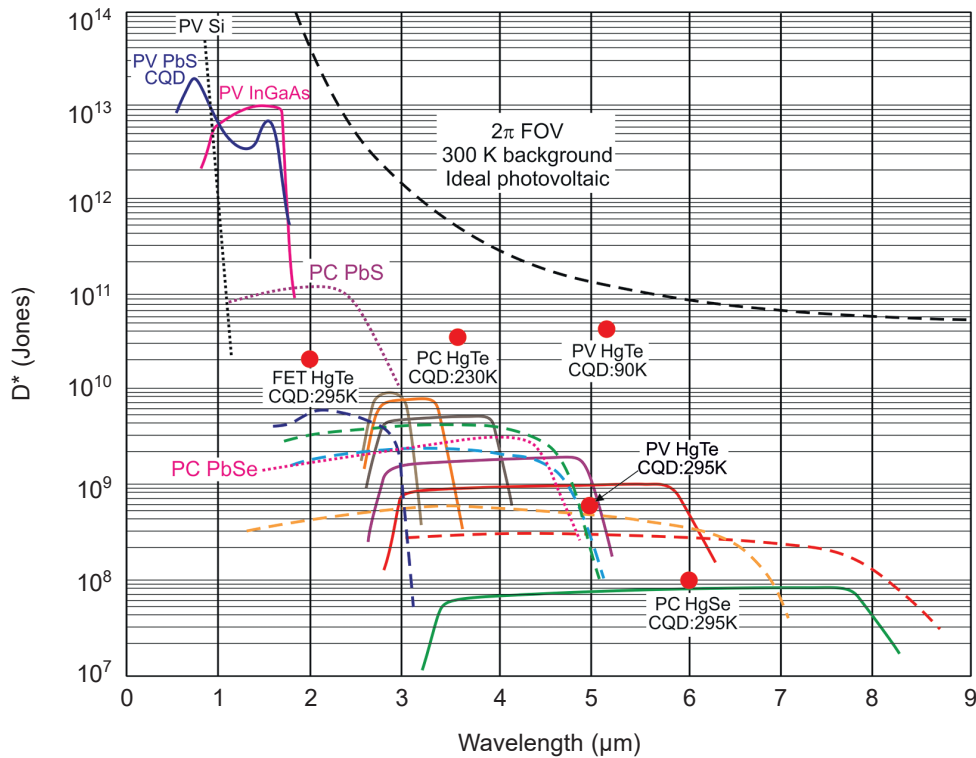


Fig. 7. Room-temperature spectral detectivity curves of the commercially available photodetectors [PV Si and InGaAs, PC PbS and PbSe, HgCdTe photodiodes (solid lines)]. The experimental data for different types of CQD photodetectors are marked by dot points [11, 38 and 41]. Also spectral detectivity of new emerging T2SL IB QCIPs are included [40]. PC – photoconductor, PV – photodiode

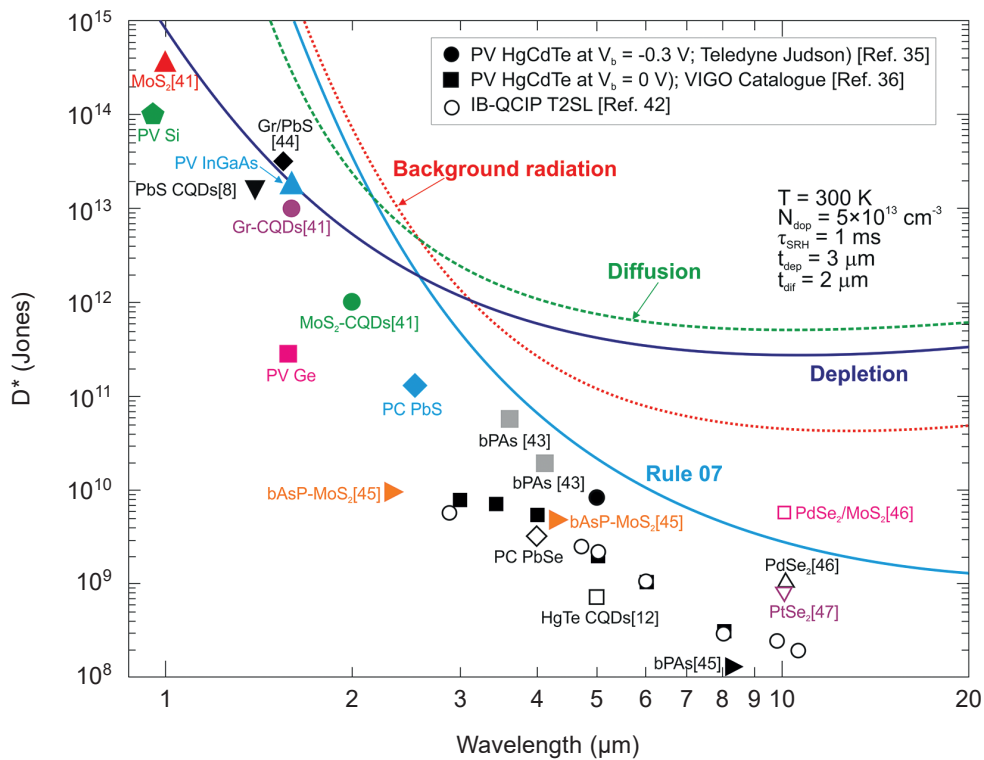


Fig. 8. Dependence of detectivity for the currently employed room-temperature operating HOT infrared photodetectors (PV Si and Ge, PV InGaAs, PC PbS and PbSe, PV HgCdTe), IB QCIP T2SLs, and CQD photodetectors (HgTe and PbS CQDs). The theoretical curves are calculated assuming the value of $\tau_{SRH} = 1$ ms and absorber doping level of $5 \times 10^{13} \text{ cm}^{-3}$. Thickness of active region is $t = 5 \text{ μm}$ and consists of $t_{dif} = 2 \text{ μm}$ and $t_{dep} = 3 \text{ μm}$. The experimental data are taken from literature as marked. PC – photoconductor, PV – photodiode

PbS and HgTe CQD photodetectors integration in camera imaging have been demonstrated [20]. Figure 8 also presents spectral D^* curves of commercially available IR photodetectors operating at room temperature together with Johnson-noise limited D^* of new emerging IB QCIPs fabricated using InAs/GaSb T2SLa absorbers. HgCdTe is currently the most commonly used variable gap semiconductor for IR photodetectors, including HOT conditions. We can see that performance of HgCdTe photodiodes and T2SL IB QCIB are comparable. It should be mentioned here that due to strong covalent bonding of III–V compounds, IB QCIPs can operate at temperatures of up to 400°C, which is not possible with the HgCdTe counterpart due to strong interdiffusion processes.

All experimental data gathered in Figs. 7 and 8 indicates photodetectors performance on sub-BLIP. Both figures also clearly show that the detectivity values of CQD photodetectors are inferior in comparison with HgCdTe photodiodes. They are generally worse also in comparison with 2D material photodetectors [black phosphorus-arsenic (bPAs) and noble transition metal dichalcogenide photodetectors like PdSe₂/MoS₂ heterojunction]. The theoretical predictions indicate a possible further performance improvement of HgCdTe devices after decreasing of i-doping level in P-i-N photodiodes. For doping level of $5 \times 10^{13} \text{ cm}^{-3}$ the photodiode performance can be limited by background radiation in spectral band above 3 μm. It is shown that in this spectral region, the D^* is not limited by detector itself, but by background photon noise at a level above 10^{10} Jones in LWIR range (above one order of magnitude above Rule 07).

5. Conclusions

In the last decade considerable progress in fabrication of SW and MWIR CQD photodetectors has been demonstrated together with their integration into thermal imaging cameras. At present stage of technology, the performance of CQD photodetectors is inferior in comparison with HgCdTe photodiodes. It seems that, the PbS CQD photodetectors characterized by multispectral sensitivity and detectivity comparable to InGaAs devices (which are currently the most common in commercial applications) have been located at the best position in IR material family at present time.

In spite of sixty years development history of HgCdTe ternary alloy system, its ultimate HOT performance limit has not been achieved. To achieve this goal, the doping concentration below $5 \times 10^{13} \text{ cm}^{-3}$ is required. This level of doping concentration has been recently achieved in fully-depleted HgCdTe FPAs by Teledyne Technologies [31].

The semiempirical rule Rule 07 (specified in 2007), widely popular in IR community as a reference for other technologies, was found not to fulfil primary expectations. In this paper it is shown that the detectivity of low-doping P-i-N HgCdTe ($5 \times 10^{13} \text{ cm}^{-3}$) photodiodes, operating at room-temperature in LWIR spectral region, is limited by background radiation and can be improved by more than one order of magnitude in comparison with that predicted by Rule 07. Between different material systems used in fabrication of HOT LWIR photodetectors,

only HgCdTe ternary alloy can fulfil required expectations: low doping concentration – 10^{13} cm^{-3} and high SRH carrier lifetime – above 1 ms. In this context it will be rather difficult to rival CQD photodetectors with HgCdTe photodiodes. The above estimates provide further encouragement for achieving low-cost and high performance MWIR and LWIR HgCdTe focal plane arrays operated in HOT conditions.

Appendix

Doping dependence relation between diffusion and depletion currents for an ideal P-i-N HgCdTe photodiode

The diffusion current arises from the thermal generation of carriers in thick, undepleted absorber [41, 42]. The diffusion current density dependent on the Auger and SRH generation in n-type semiconductor is equal

$$J_{dif} = \frac{qn_i^2 t_{dif}}{n} \left(\frac{1}{\tau_{A1}} + \frac{1}{\tau_{SRH}} \right), \quad (A1)$$

where q stands for the electron charge, n is the electron concentration, t_{dif} is the diffusion region thickness, n_i is the intrinsic carrier concentration, τ_{A1} is the Auger 1 lifetime, and τ_{SRH} is the SRH lifetime. Auger 1 lifetime is related to the hole, electron, and intrinsic carrier concentrations, and τ_{A1} is given by equation

$$\tau_{A1} = \frac{2\tau_{A1}^i n_i^2}{n(n+p)}, \quad (A2)$$

where p is the hole concentration and τ_{A1}^i is the intrinsic Auger 1 lifetime. For a low temperature operation or a non-equilibrium active volume, when the majority carrier concentration is held equal to the majority carrier doping level [and intrinsically generated majority carriers are excluded ($p \ll n \approx N_{dop}$)], Eq. (A2) becomes

$$\tau_{A1} = \frac{2\tau_{A1}^i n_i^2}{n^2}. \quad (A3)$$

The shortest SRH lifetime occurs through centres located approximately at the intrinsic energy level in the semiconductor bandgap. Then, for the field-free region in an n volume ($n \gg p$), τ_{SRH} is given by

$$\tau_{SRH} = \frac{\tau_{no} n_i + \tau_{po}(n + n_i)}{n}, \quad (A4)$$

where $n \approx n_i$, we have $\tau_{SRH} \approx \tau_{no} + \tau_{po}$. For a non-equilibrium active volume, $\tau_{SRH} \approx (\tau_{no} + \tau_{po})n_i/n$ exhibits a temperature dependence given by n_i .

A comparison of the Auger 1 and SRH lifetimes in equilibrium and non-equilibrium modes is shown in Fig. A1 for

Comparison of performance limits of the HOT HgCdTe photodiodes with colloidal quantum dot infrared detectors

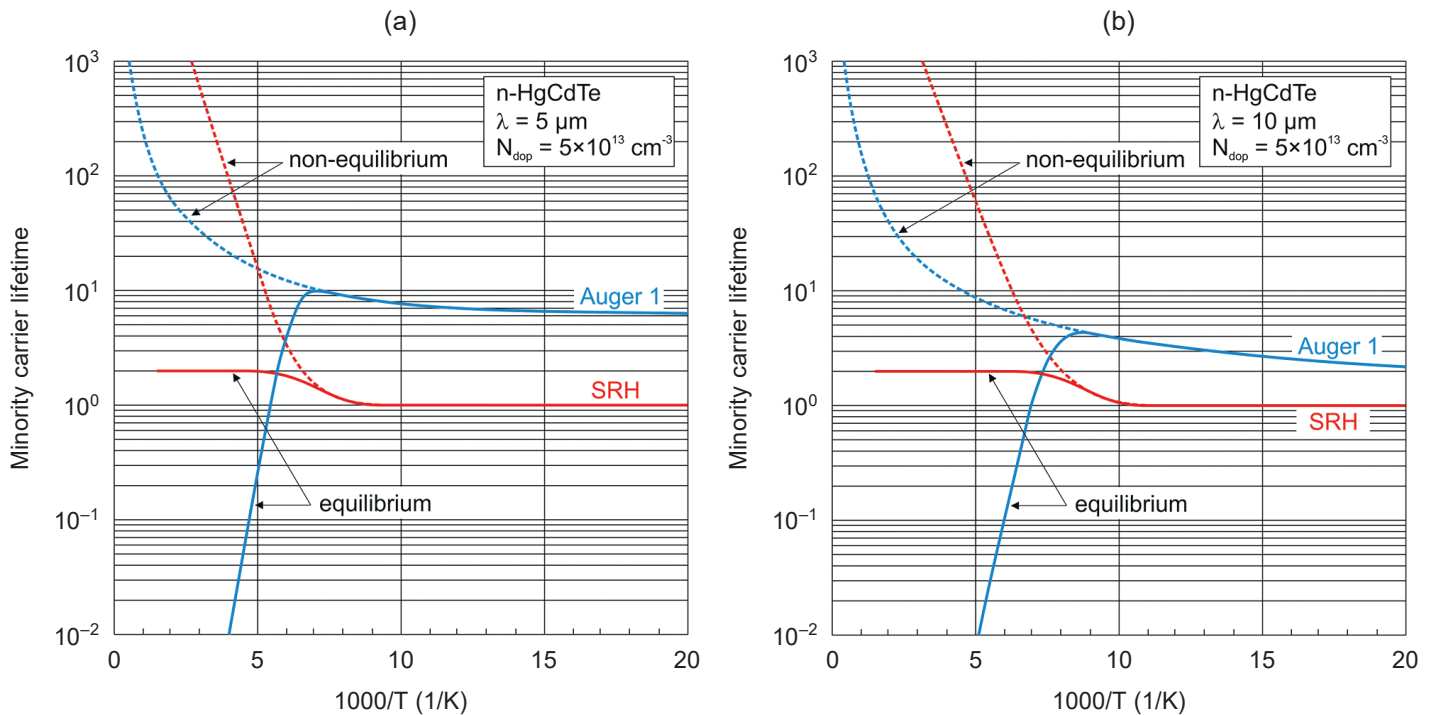


Fig. A1. Equilibrium and non-equilibrium Auger1 and SRH minority carrier lifetime versus inverse temperature for MWIR and LWIR HgCdTe with n-type doping concentration of $5 \times 10^{13} \text{ cm}^{-3}$.

MWIR ($\lambda_c = 5 \mu\text{m}$) and LWIR ($\lambda_c = 10 \mu\text{m}$) HgCdTe with n-type doping concentration of $5 \times 10^{13} \text{ cm}^{-3}$. In calculations the Hansen and Schmit analytical expression for the intrinsic carrier concentration was used [48]. The strong increase of SRH lifetimes for non-equilibrium mode of operation in high temperature is caused by the decreasing electron population of the SRH level, which in consequence results in the decreasing of the minority carriers capture rates [27].

The second component is the depletion current arising from the portion of the absorber that becomes depleted. The depletion current density can be estimated by the following expression

$$J_{dep} = \frac{qn_i t_{dep}}{\tau_{no} + \tau_{po}}, \quad (A5)$$

where t_{dep} is the width of depletion region.

Figure A2 shows the calculated reverse bias voltage which is required to completely deplete a 5- μm -thick absorber doped at different doping level. For the Rule 7 doping range, a 5- μm -thick absorber can be fully depleted by applying a relatively high reverse bias between 10 V and 30 V. On the other hand, for the range of doping reached presently at Teledyne, the 5- μm -thick absorber can be fully depleted for reverse bias from zero up to 0.4 V.

So far, for achievable doping levels there is a visible transition between the diffusion and depletion current domination for so-called knee temperature, T_{knee} . At low temperatures, where $n_i \ll N_{dop}$, the depletion component is dominant ($J_{dif} \ll J_{dep}$), and the presence of the depletion region determines the device

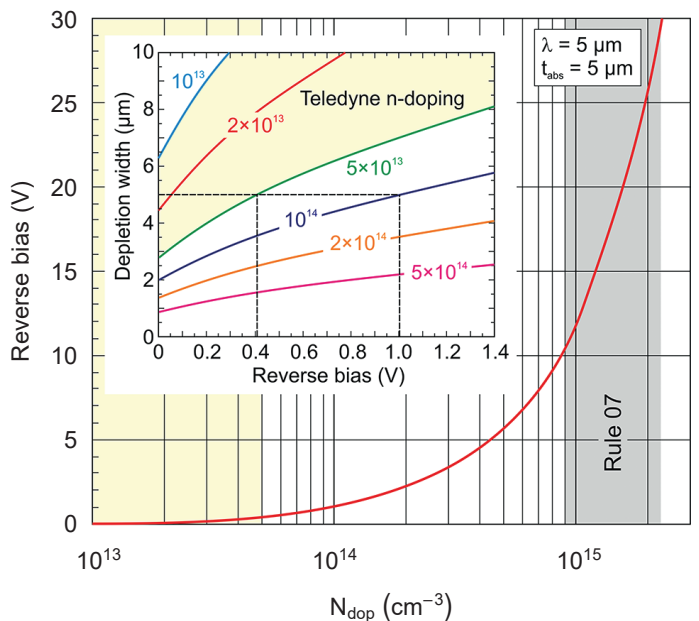


Fig. A2. Calculated reverse bias voltage versus doping concentration required to deplete a 5- μm -thick MWIR HgCdTe absorber. Inset: Width of absorber depletion versus reverse bias voltage and doping concentration

performance. At high temperatures, where $n_i \gg N_{dop}$, the presence of the depletion region does not limit the device performance. The knee temperature, T_{knee} , between depletion domination at low temperature and diffusion domination at high

temperature can be specified assuming $J_{dif} = J_{dep}$. In our considerations we have assumed an identical carrier lifetimes for both currents, assuming τ as a minority carrier lifetime. We can then express the diffusion current density at equilibrium and the depletion current density as

$$J_{dif}^{eq} = \frac{qn_i^2 t_{dif}}{N_{dop} \tau}, \quad (A6)$$

$$J_{dep} = \frac{qn_i t_{dep}}{\tau}. \quad (A7)$$

Considering Auger 1 suppression, the only relevant diffusion dark current component is SRH diffusion current with density expressed as

$$J_{dif}^{non-eq} = \frac{qn_i^2 t_{dif}}{(N_{dop} + 2n_i) \tau} \quad (A8)$$

According to Fig. A2, the assumption of an equivalent volume for depletion and diffusion regions ($t_{dif} = t_{dep}$), as presented by Gravrand et al. [30], is in general not valid. In our calculations we assumed the relation between the diffusion region thickness the depletion width as $t_{dif} = t_{abs} - t_{dep}$, where t_{abs} is the absorber thickness, taken as 5 μm in calculations. Figure A3 shows diffusion-depletion knee temperature versus doping level in n-type absorption region for P-on-n double layer photodiode (DLPH) and P-i-N HgCdTe photodiodes with cut-off wavelengths equal 5 and 10 μm .

Fig. A3 allows to draw the following conclusions:

- for photodiodes with the longer cut-off wavelength, the knee temperature is lower,

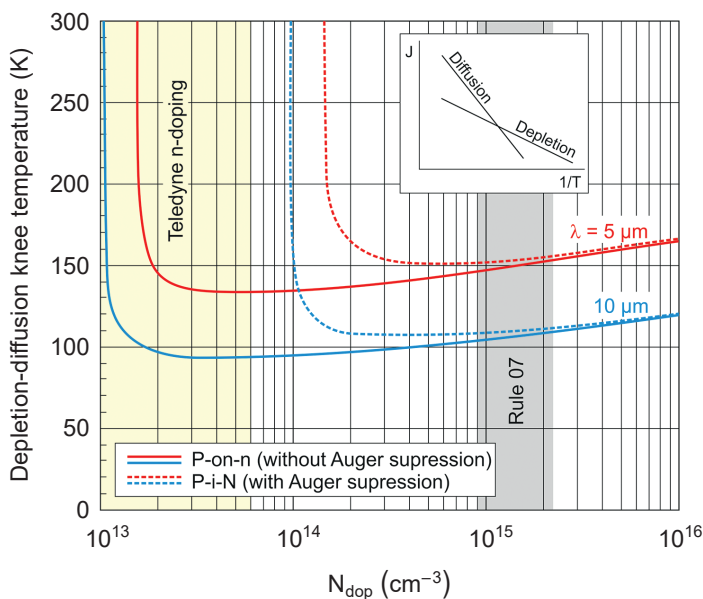


Fig. A3. Depletion-diffusion knee temperature versus doping level in n-type absorption region for HgCdTe P-on-n and P-i-N photodiodes with cut-off wavelengths equal 5 and 10 μm

- at a very low doping (10^{13} cm^{-3}) there is no visible knee temperature since a 5- μm -thick absorber is completely depleted,
- Auger suppression causes that the depletion current becomes dominant for doping concentrations below 10^{14} cm^{-3} .

Acknowledgements. This paper has been completed with the financial support of the Polish National Science Centre: 2018/31/B/ST7/01541, 2018/30/M/ST7/00174, and 2017/27/B/ST7/01507.

REFERENCES

- [1] O. Iwert and B. Delabrea, “The challenge of highly curved monolithic imaging detectors”, *Proc. SPIE* 7742, 774227–1–9 (2010).
- [2] K.-H. Jeong, J. Kim, and L.P. Lee, “Biologically inspired artificial compound eyes”, *Science* 312, 557–561 (2006).
- [3] Y.M. Song, Y. Xie, V. Malyarchuk, J. Xiao, I. Jung, K.-J. Choi, Z. Liu, H. Park, C. Lu, R.H. Kim, R.Li, K.B. Crozier, Y. Huang, and J.A. Rogers, “Digital cameras with designs inspired by the arthropod eye,” *Nature* 497(7447), 95–99 (2013).
- [4] X. Tang, M.M. Ackerman, and P. Guyot-Sionnest, “Colloidal quantum dots based infrared electronic eyes for multispectral imaging”, *Proc. SPIE* 11088, 1108803–1–7 (2019).
- [5] P. Martyniuk, S. Krishna, and A. Rogalski, “Assessment of quantum dot infrared photodetectors for high temperature operation”, *J. Appl. Phys.* 104(3), 034314–1–6 (2008).
- [6] D. Lee, M. Carmody, E. Piquette, P. Dreiske, A. Chen, A. Yulius, D. Edwall, S. Bhargava, M. Zandian, and W.E. Tennant, “High-operating temperature HgCdTe: A vision for the near future”, *J. Electron. Mater.* 45(9), 4587–4595 (2016).
- [7] A.D. Stiff-Roberts, “Quantum-dot infrared photodetectors: a review”, *J. Nanophoton.*, 3, 031607 (2009).
- [8] G. Konstantatos and E.H. Sargent, “Solution-processed quantum dot photodetectors”, *Proc. IEEE* 97(10), 1666–1683 (2009).
- [9] N.C. Greenham, X. Peng, and A.P. Alivisatos, “Charge separation and transport in conjugated polymer/cadmium selenide nanocrystal composites studied by photoluminescence quenching and photoconductivity”, *Syn. Met.* 84, 545-546 (1997).
- [10] D.S. Ginger and N.C. Greenham, “Photoinduced electron transfer from conjugated polymers to CdSe nanocrystals”, *Phys. Rev. B* 59, 10622–10629 (1999).
- [11] F.P. Garcia de Arquer, A. Armin, P. Meredith, and E.H. Sargent, “Solution-processed semiconductors for next-generation photodetectors”, *Nat. Rev. Mater.* 2, 16100 (2017).
- [12] P. Guyot-Sionnest, M.M. Ackerman, and X. Tang, “Colloidal quantum dots for infrared detection beyond silicon”, *J. Chem. Phys.* 151, 060901–1–8 (2019).
- [13] P. Guyot-Sionnest and J.A. Roberts, “Background limited mid-infrared photodetection with photovoltaic HgTe colloidal quantum dots”, *Appl. Phys. Lett.* 107, 091115 (2015).
- [14] C. Buurma, R.E. Pimpinella, A.J. Ciani, J.S. Feldman, C.H. Grein, and P. Guyot-Sionnest, “MWIR imaging with low cost colloidal quantum dot films”, *Proc. SPIE* 9933, 993303 (2016).
- [15] C. Buurma, A.J. Ciani, R.E. Pimpinella, J.S. Feldman, C.H. Grein, and P. Guyot-Sionnest, “Advances in HgTe colloidal quantum dots for infrared detectors”, *J. Electron. Mater.* 46(11) 6685–6688 (2017).
- [16] E.J.D. Klem, C. Gregory, D. Temple, and J. Lewis, “PbS colloidal quantum dot photodiodes for low-cost SWIR sensing”, *Proc. SPIE* 9451, 945104–1–5 (2015).

Comparison of performance limits of the HOT HgCdTe photodiodes with colloidal quantum dot infrared detectors

- [17] A. De Iacovo, C. Venettacci, L. Colace, L. Scopa, and S. Foglia, "PbS Colloidal Quantum Dot Photodetectors operating in the near infrared", *Sci. Rep.* 6, 37913 (2016).
- [18] M. Thambidurai, Y. Jjang, A. Shapiro, G. Yuan, H. Xiaonan, Y. Xuechao, G. J. Wang, E. Lifshitz, H. V. Demir, and C. Dang, "High performance infrared photodetectors up to 2.8 μm wavelength based on lead selenide colloidal quantum dots", *Opt. Mater. Express* 7(7), 2336 (2017).
- [19] P.E. Malinowski, E. Georgitzikis, J. Maes, I. Vamvaka, F. Frazzica, J. Van Olmen, P. De Moor, P. Heremans, Z. Hens, and D. Cheyns, "Thin-film quantum dot photodiode for monolithic infrared image sensors", *Sensors* 17, 2867 (2017).
- [20] S.B. Hafiz, M. Scimeca, A. Sahu, and D.-K. Ko, "Colloidal quantum dots for thermal infrared sensing and imaging", *Nano Convergence* 6, 7 (2019).
- [21] SWIR Vision Systems, AcurosTM, CQDTM, SWIR Cameras: https://ibv.vdma.org/documents/256550/27019077/2018-11-07_Stage1_1030_SWIR+Vision+Systems.pdf
- [22] Imec develops infrared thin-film sensor with 'record' pixel density, 23 Oct 2019, <https://optics.org/news/10/10/38>
- [23] C.T. Elliott, N.T. Gordon, and A.M. White, "Towards background-limited, room-temperature, infrared photon detectors in the 3–13 mm wavelength range", *Appl. Phys. Lett.* 74(9), 2881-2883 (1999).
- [24] J. Robinson, M. Kinch, M. Marquis, D. Littlejohn, and K. Jeppson, "Case for small pixels: system perspective and FPA challenge", *Proc. SPIE* 9100, 91000I-1-10 (2014).
- [25] A. Rogalski, P. Martyniuk and M. Kopytko, "Challenges of small-pixel infrared detectors: a review", *Rep. Prog. Phys.* 79, 046501-1-42 (2016).
- [26] G.C. Holst and T.C. Lomheim, *CMOS/CCD Sensors and Camera Systems*, JCD Publishing and SPIE Press, Winter Park, (2007).
- [27] M.A. Kinch, *State-of-the-Art Infrared Detector Technology*, SPIE Press, Bellingham, 2014.
- [28] G.C. Holst and R.G. Driggers, "Small detectors in infrared system design", *Opt. Eng.* 51(9), 096401-1-10 (2012).
- [29] M.S. Kinch, F. Aqariden, D. Chandra, P.-K. Liao, H.F. Schaake, and H.D. Shih, "Minority carrier lifetime in p-HgCdTe", *J. Electron. Mater.* 34, 880–884 (2005).
- [30] O. Gravrand, J. Rothman, B. Delacourt, F. Boulard, C. Lobre, P.H. Ballet, J.L. Santailler, C. Cervera, D. Brellier, N. Pere-Laperne, V. Destefanis, and A. Kerlain, "Shockley-Read-Hall lifetime study and implication in HgCdTe photodiodes for IR detection", *J. Electron. Mater.* 47(10), 5680–5690 (2018).
- [31] D. Lee, P. Dreiske, J. Ellsworth, R. Cottier, A. Chen, S. Tallarico, H. Barr, H. Tcheou, A. Yulius, M. Carmody, E. Piquette, M. Zandian, and S. Douglu, "Performance of MWIR and LWIR fully-depleted HgCdTe FPAs", Extended Abstracts. The 2019 U.S. Workshop on the Physics and Chemistry of II–VI Materials, pp. 189–190.
- [32] A. Rogalski, M. Kopytko, and P. Martyniuk, "Performance prediction of p-i-n HgCdTe long-wavelength infrared HOT photodiodes", *Appl. Opt.* 57(18) D11–D19 (2018).
- [33] T. Ashley and C. T. Elliott, "Non-equilibrium mode of operation for infrared detection," *Electron. Lett.* 21(10), 451–452 (1985).
- [34] C.T. Elliott, "Non-equilibrium mode of operation of narrow-gap semiconductor devices", *Semicond. Sci. Technol.* 5, S30–7 (1990).
- [35] HOT MCT Detectors, <http://www.teledynejudson.com/>
- [36] VIGO System product catalog, <https://vigo.com.pl/wp-content/uploads/2017/06/VIGO-Catalogue.pdf>
- [37] W. Huang, S.M.S. Rassela, L. Li, J.A. Massengale, R.Q. Yang, T.D. Mishima, and M.B. Santos, "A unified figure of merit for interband and intersubband cascade devices", *Infrared Phys. Technol.* 96, 298–301 (2019)
- [38] E. Lhuillier and P. Guyot-Sionnest, "Recent progress in mid infrared nanocrystal optoelectronics", *IEEE J. Selected Topics in Quantum Electronics* 23(5), 6000208 (2017).
- [39] M. Chen, H. Lu, N. M. Abdelazim, Y. Zhu, Z. Wang, W. Ren, S.V. Kershaw, A.L. Rogach, and N. Zhao, "Mercury telluride quantum dot based phototransistor enabling high-sensitivity room-temperature photodetection at 2000 nm", *ACS Nano* 11, 5614–5622 (2017).
- [40] C. Livache, B. Martinez, N. Goubet, J. Ramade, and E. Lhuillier, "Road map for nanocrystal based infrared photodetectors", *Front. Chem.* 6, 575 (2018).
- [41] G. Konstantatos, "Current status and technological prospect of photodetectors based on two-dimensional materials", *Nat. Commun.* 9, 5266 (2018).
- [42] A. Rogalski, P. Martyniuk, and M. Kopytko, "Type-II superlattice photodetectors versus HgCdTe photodiodes", *Prog. Quant. Electron.* 68, 100228 (2019).
- [43] M. Amani, E. Regan, J. Bullock, G.H. Ahn, and A. Javey, "Mid-wave infrared photoconductors based on black phosphorus-arsenic alloys", *ACS Nano* 11, 11724-11731 (2017).
- [44] G. Konstantatos, M. Badioli, L. Gaudreau, J. Osmond, M. Bernechea, F.P. Garcia de Arquer, F. Gatti, and F.H.L. Koppens "Hybrid graphene-quantum dot phototransistors with ultrahigh gain", *Nat. Nanotechnol.* 7, 363–368 (2012).
- [45] M. Long, A. Gao, P. Wang, H. Xia, C. Ott, C. Pan, Y. Fu, E. Liu, X. Chen, W. Lu, T. Nilges, J. Xu, X. Wang, W. Hu, and F. Miao, "Room temperature high-detectivity mid-infrared photodetectors based on black arsenic phosphorus", *Sci. Adv.* 3, 700589 (2017).
- [46] M. Long, Y. Wang, P. Wang, X. Zhou, H. Xia, C. Luo, S. Huang, G. Zhang, H. Yan, Z. Fan, X. Wu, X. Chen, W. Lu, and W. Hu, "Palladium diselenide long-wavelength infrared photodetector with high sensitivity and stability", *ACS Nano* 13, 2511–2519 (2019).
- [47] X. Yu, P. Yu, D. Wu, B. Singh, Q. Zeng, H. Lin, W. Zhou, J. Lin, K. Suenaga, Z. Liu, and Q.J. Wang, "Atomically thin noble metal dichalcogenide: a broadband mid-infrared semiconductor", *Nat. Commun.* 9, 1545 (2018).
- [48] G.L. Hansen and J.L. Schmit, "Calculation of intrinsic carrier concentration in $\text{Hg}_{1-x}\text{Cd}_x\text{Te}$ ", *J. Appl. Phys.* 54, 1639–1640 (1983).